Mg/ZrO$_2$ Metal Matrix Nanocomposites Fabricated by Friction Stir Processing: Microstructure, Mechanical Properties, and Corrosion Behavior

Ke Qiao[1]*, Ting Zhang[1], Kuaishe Wang[1], Shengnan Yuan[1], Shengyi Zhang[1], Liqiang Wang[2], Zhi Wang[1], Pai Peng[1], Jun Cai[1], Chaozong Liu[3]* and Wen Wang[1]*

[1] School of Metallurgical Engineering, National and Local Joint Engineering Research Center for Functional Materials Processing, Xi'an University of Architecture and Technology, Xi'an, China, [2] State Key Laboratory of Metal Matrix Composites, School of Materials Science and Engineering, Shanghai Jiao Tong University, Shanghai, China, [3] Institute of Orthopaedics and Musculoskeletal Science, University College London, Royal National Orthopaedic Hospital, Stanmore, United Kingdom

Magnesium (Mg) and its alloys have attached more and more attention because of their potential as a new type of biodegradable metal materials. In this work, AZ31/ZrO$_2$ nanocomposites with good uniformity were prepared successfully by friction stir processing (FSP). The scanning electron microscope (SEM) and transmission electron microscope (TEM) were used to characterize the microstructure of the composites. The mechanical properties, electrochemical corrosion properties and biological properties were evaluated. In addition, the effect of reinforced particles (ZrO$_2$) on the microstructure and properties of the composite was studied comparing with FSP AZ31 Mg alloy. The results show that compared with the base metal (BM), the AZ31/ZrO$_2$ composite material achieves homogenization, densification, and grain refinement after FSP. The combination of dynamic recrystallization and ZrO$_2$ particles leads to grain refinement of Mg alloy, and the average grain size of AZ31/ZrO$_2$ composites is 3.2 μm. After FSP, the c-axis of grain is deflected under the compression stress of shoulder and the shear stress of pin. The ultimate tensile strength (UTS) and yield strength (YS) of BM were 283 and 137 MPa, respectively, the UTS and YS of AZ31/ZrO$_2$ composites were 427 and 217 MPa, respectively. The grain refinement and Orowan strengthening are the major strengthening mechanisms. Moreover, the corrosion resistance in simulated body fluid of Mg alloy is improved by grain refinement and the barrier effect of ZrO$_2$.

Keywords: Friction stir processing, microstructure, mechanical properties, corrosion properties, texture

INTRODUCTION

Magnesium (Mg) and its alloys are considered to have great potential in biomedical application due to the high strength-to-weight ratio, good biocompatibility and promotion of bone cell healing (Staiger et al., 2006; Castellani et al., 2011; Henderson et al., 2014). However, the high corrosion and degradation rates *in vivo*, and the low strength limit their application development

(Morisada et al., 2006a). Previous studies have shown that the Mg matrix composites prepared by adding secondary particles to Mg can significantly reduce the corrosion and degradation rates, thus improve strength, corrosion resistance, and biocompatibility (Lan et al., 2004; Wang et al., 2004; Ugandhar et al., 2006).

At present, powder metallurgy (Davis and Ward, 1993), in-situ fabrication (Daniel et al., 1997), spray deposition (Lavernia and Grant, 1988), and stir casting (Hashim et al., 1999) are commonly used to fabricate composites. However, the composites fabricated by the above methods have many defects such as voids, which is eliminated by severe plastic deformation methods such as extrusion and rolling, leading to a longer process and higher cost. Therefore, it is necessary to develop an effective technique to prepare high-quality composites.

Friction stir processing (FSP) is an alternative solid-state processing technology for producing Mg matrix composites, based on the principles of friction stir welding (FSW), potentially addressing the above-mentioned limitations (Mishra and Ma, 2005). Specifically, FSP can achieve the homogenization, densification, and grain refinement of microstructure simultaneously (Ammouri et al., 2015; Ni et al., 2016; Xu and Bao, 2016), thus improve the mechanical properties and corrosion properties of materials. In 2006, Morisada et al. (2006b) first prepared AZ31/MWCNTs (multi-walled carbon nanotubes) surface composites by FSP. It was reported that the low temperature could avoid the interfacial reaction between reinforced particles and Mg matrix during FSP. Furthermore, severe plastic deformation contributed to the fragment and uniform mixing of reinforced particles. This work has attracted many research interests in the preparation of Mg matrix composites by FSP.

So far, a lot of reinforced particles, such as TiC (Balakrishnan et al., 2015; Navazani and Dehghani, 2015), TiAlC (Gobara et al., 2015), Al$_2$O$_3$ (Azizieh et al., 2018), B$_4$C (Vedabouriswaran and Aravindan, 2018), MWCNT (Morisada et al., 2006b; Arab et al., 2017), and SiC (Morisada et al., 2006a) have been added in Mg matrix by FSP, improving the mechanical properties of the alloys. For example, Navazani and Dehghani (2015) and Balakrishnan et al. (2015) studied the microstructure and mechanical properties of AZ31/TiC composites fabricated by FSP. The results showed that TiC particles distributed uniformly in AZ31 Mg matrix after FSP, which promoted the grain refinement and improved the microhardness. According to the research of Azizieh et al. (2018), adding Al$_2$O$_3$ to AZ31 Mg alloy with FSP effectively increased the wear resistance of the material. It has been reported (Vedabouriswaran and Aravindan, 2018) that after adding B$_4$C particles to RZ 5 Mg alloy, the coarse grains in base metal (BM) become the fine grains in composites due to the pinning effect of reinforced particles. The microhardness and tensile strength from 81 HV and 200 MPa (BM) increased to 403 HV and 320 MPa (composites), respectively. This phenomenon also be founded in AZ31/SiC composites fabricated by FSP (Morisada et al., 2006a). However, there are few reports on the above-mentioned reinforcing particles for improving biocompatibility of Mg alloys, it is vital to find other materials to address the above problem.

Studies have shown that the addition of ZrO$_2$ particles in Mg matrix contributes to the mechanical properties and biocompatibility of materials (Navazani and Dehghani, 2016; Vignesh et al., 2019). For example, Navazani and Dehghani (2016) added ZrO$_2$ particles to AZ31 Mg plate through FSP, then observed that the particles promote the grain refinement and improve the mechanical properties of composites. Vignesh et al. (2019) prepared AZ91D-ZrO$_2$ surface composites by FSP. It was reported that the combination of FSP and ZrO$_2$ reduced the grain size, and broke and disperse the secondary particles. The dispersion of ZrO$_2$ particles can increase the accumulated surface potential, thereby improving the corrosion resistance of composites. However, only simply characterize and evaluate the microstructure and performance of ZrO$_2$/Mg matrix composites in previous researches, the influence mechanism of microstructure on mechanical properties and corrosion resistance has not been thoroughly and comprehensively analyzed and discussed.

In view of the above problems, AZ31/ZrO$_2$ nanocomposites are prepared in this work by FSP. The microstructure, mechanical properties, and corrosion resistance of AZ31 Mg alloy and AZ31/ZrO$_2$ nanocomposites are analyzed in detail to clary the influence of FSP and ZrO$_2$ particles on the Mg alloy, respectively. The present work intends to provide a new insight for the preparation of biomedical Mg matrix composites.

MATERIALS AND EXPERIMENTAL METHODS

Materials Preparation

A rolled AZ31 Mg plate with a dimension of 100 mm × 80 mm × 3 mm was used as Base metal (BM) in this work. ZrO$_2$ powder with a diameter ranging from 50 to 150 nm and an average diameter of 80 nm was used as reinforcement as shown in **Figure 1**. The volume fraction of the ZrO$_2$ particles added to the plate is about 17.6%. Holes with diameter of 3 mm, depth of 1 mm and hole spacing of 10 mm were drilled by a drilling machine on the surface of the AZ31 Mg alloy plates. After filling the prefabricated holes with ZrO$_2$ particles, these plates were processed by FSP. The AZ31 Mg alloy plates with and without ZrO$_2$ particles were processed on a FSP machine (LM-BM16), respectively. The stir tool consisting of cylindrical shoulder of 20 mm in diameter, pin of 2 mm in length and 4 mm in diameter. The tool rotation speed was 1180 rpm, the processing speed was 23.5 mm/min, the tilt angle was 2° and the plunge depth was 0.5 mm. All samples were processed six passes. The schematic of the FSP is shown in **Figure 2**. Here into, AZ31 Mg alloy sample without ZrO$_2$ particles by FSP is marked as FSP, and the AZ31 Mg alloy sample with ZrO$_2$ particles is marked as FSP-ZrO$_2$.

Microstructural Characterization

Metallographic specimens were taken along the perpendicular PD with a dimension of 20 mm × 5 mm × 3 mm, which were grinded, polished, and etched by picric acid etching

FIGURE 1 | SEM micrograph of ZrO$_2$ powder.
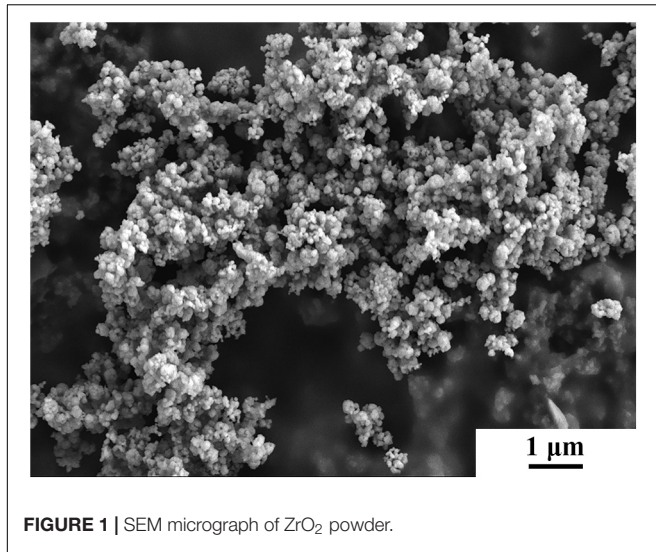
then the twin-jet electropolishing was conducted using 6% perchloric acid ethanol solution at $-30°$C. TEM observations were performed on JEM-200CX equipment at a voltage of $\sim$120 kv.
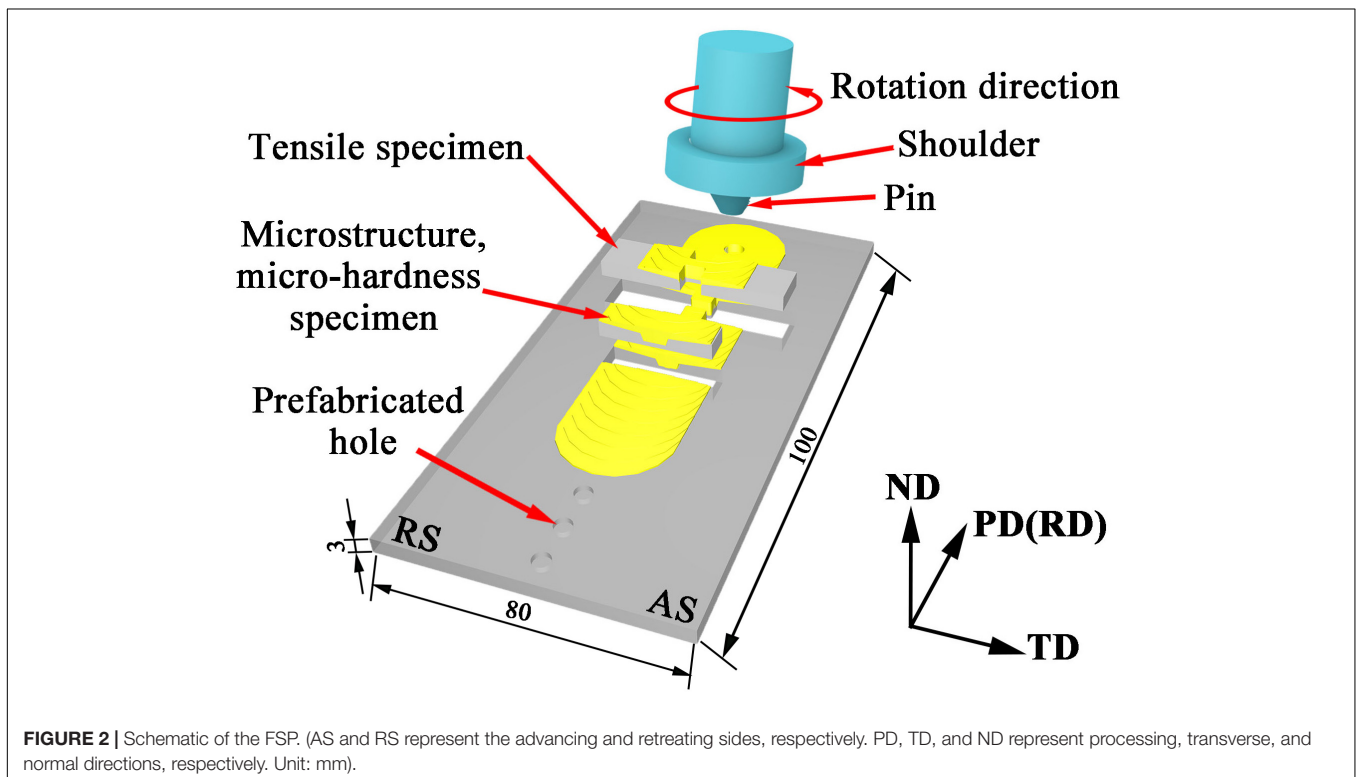
Mechanical Properties

The hardness sample with the dimension of 20 mm $\times$ 5 mm $\times$ 3 mm were cut along the vertical PD. The hardness testing was carried on the TD $\times$ ND plane using a 401MVD microhardness tester with a loading of 100 g and a dwell time of 10 s. Indentations spacing were 0.5 mm in this work. The tensile specimens with a gauge section dimension of 34 mm $\times$ 8 mm $\times$ 3 mm were cut along PD, ground and polished, then tested on an Instron 8,801 equipment at room temperature. The strain rate was 1.0×10^{-3} s^{-1}. Each testing was repeated at least three times to ensure the accuracy of data. The fracture surfaces of tensile specimens were characterized by SEM.

Electrochemical Corrosion Performance

The electrochemical corrosion samples with a dimension of 8 mm $\times$ 8 mm $\times$ 3 mm were cut from BM, FSP (SZ), and FSP-ZrO$_2$ (SZ). After grinding and polishing the sample, the electrochemical test was performed on the Gamry Reference 600 + instrument. The corrosion solution was simulated body fluid (8.035 g/L). NaCl, 0.355 g/L NaHCO$_3$, 0.225 g/L KCl, 0.231 g/L K$_2$HPO$_4$·3H$_2$O, 0.311 g/L MgCl$_2$·6H$_2$O, 39 mL/L HCl (1 mol/L), 0.292 g/L CaCl$_2$, 0.072 g /L NaSO$_4$, 6.118 g/L Tris, 1 mol/L HCl) (Kokubo and Takadama, 2006). The samples

solution (10 mL acetic acid + 10 mL water + 4.2 g picric acid dissolved in 100 mL alcohol) for 10 s. The microstructures were observed using scanning electron microscope (SEM, Gemini SEM 300) with electron backscatter diffraction (EBSD) at a voltage of $\sim$5 kv. The samples were electrolytically polished in a 10 vol.% of perchloric acid solution at a voltage of $\sim$10 V and a temperature of $-20°$C. TEM samples with a dimension of 10 mm $\times$ 10 mm $\times$ 1 mm were cut from stir zone (SZ) in FSP-ZrO$_2$, and ground to a thickness of approximately to 40 μm with sandpaper, and

FIGURE 2 | Schematic of the FSP. (AS and RS represent the advancing and retreating sides, respectively. PD, TD, and ND represent processing, transverse, and normal directions, respectively. Unit: mm).
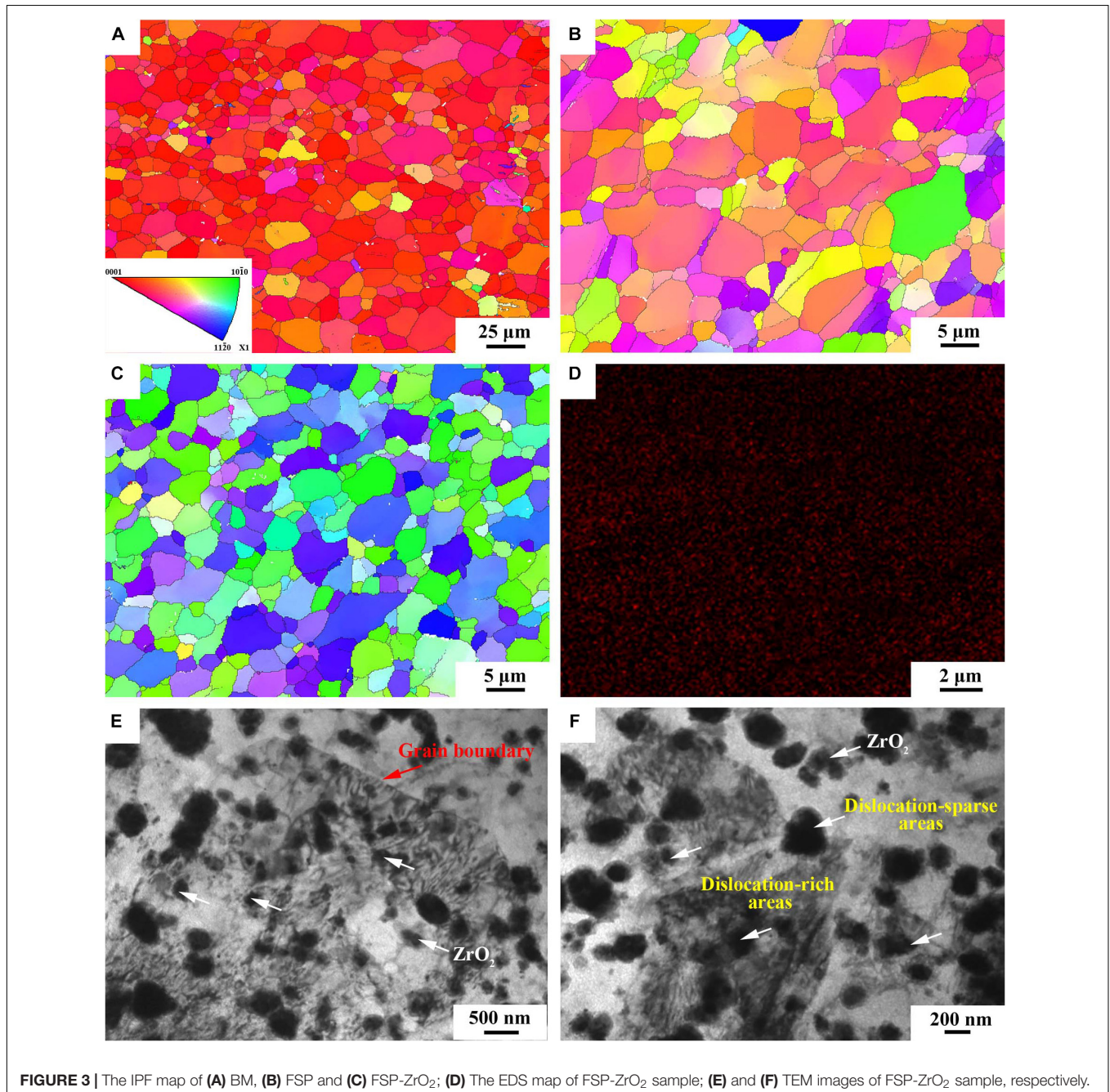
were used as the working electrodes, Ag/AgCl (saturated KCl) and platinum strip were used as the reference and counter electrodes, respectively. Before recording the potentiodynamic polarization curves, the samples were soaked in the simulated body fluid (SBF) solution for 300 s to get the steady reaction condition. The impedance measurement scan frequency ranges from 100,000 Hz to 0.1 Hz with an excitation signal amplitude is 10 mV. The impedance data were analyzed using the ZSimpWin software. The initial potential is reduced by 500 mV relative to the open circuit potential (OCP), and the termination potential is increased by 1.5 V relative to the

OCP. The scan rate is 1 mV/s, and the test temperature is room temperature.

Scanning Vibrating Electrode Technique (SVET) Measurement

The SVET samples were cut from BM, and SZ of the FSP and FSP-ZrO$_2$ samples with a dimension of 8 μm × 8 μm. After grinding and polishing, they were tested on the Princeton VersaSCAN instrument. The measurements were performed in SBF and at an OCP. The scanning range was 600 μm × 600 μm, the scanning

FIGURE 3 | The IPF map of **(A)** BM, **(B)** FSP and **(C)** FSP-ZrO$_2$; **(D)** The EDS map of FSP-ZrO$_2$ sample; **(E)** and **(F)** TEM images of FSP-ZrO$_2$ sample, respectively.

speed was 10 μm/s, and the process combined surface scanning and line scanning. The SVET samples were immersed for 1, 3, 6, and 24 h, respectively. The statistical analysis of SVET data was carried out with Origin software. The voltages were displayed in a three-dimensional (3D) maps, which showed the spatial distribution of the voltage as a function of the (x, y) position in the scan region. The voltage value in the SVET map is positive for anodic currents and negative for cathodic currents. The contour map of the voltage was located at the bottom of the 3D map.

RESULTS

Microstructure Evolution

Figures 3A–C show the inverse pole figure (IPF) of BM, FSP and FSP-ZrO$_2$ samples. BM exhibits equiaxed grains with the

size ranging from 0.2 to 53.5 μm, and the average size is 10 μm (**Figure 3A**). Compared with BM, FSP displays a more uniform microstructure and finer grain, with a grain size range of 0.1–15 μm and an average size of 4.0 μm (**Figure 3B**). The microstructure of FSP-ZrO$_2$ sample is further homogenized and refined, with a grain size range of 0.1–14 μm and an average grain size of 3.2 μm (**Figure 3C**), which indicates that ZrO$_2$ particles contribute to reducing grain size. Morisada et al. (2006a) showed that FSP with the SiC particles can refine grains more effectively due to the enhancement of the induced strain and the pinning effect by the SiC particles. Therefore, it can be considered that the ZrO$_2$ particles in this work play a similar role to the SiC particles in the report. **Figure 3D** shows the distribution of Zr elements in FSP-ZrO$_2$ sample. Zr element is uniformly distributed in the Mg matrix without obvious vacancies and aggregation, indicating that the ZrO$_2$
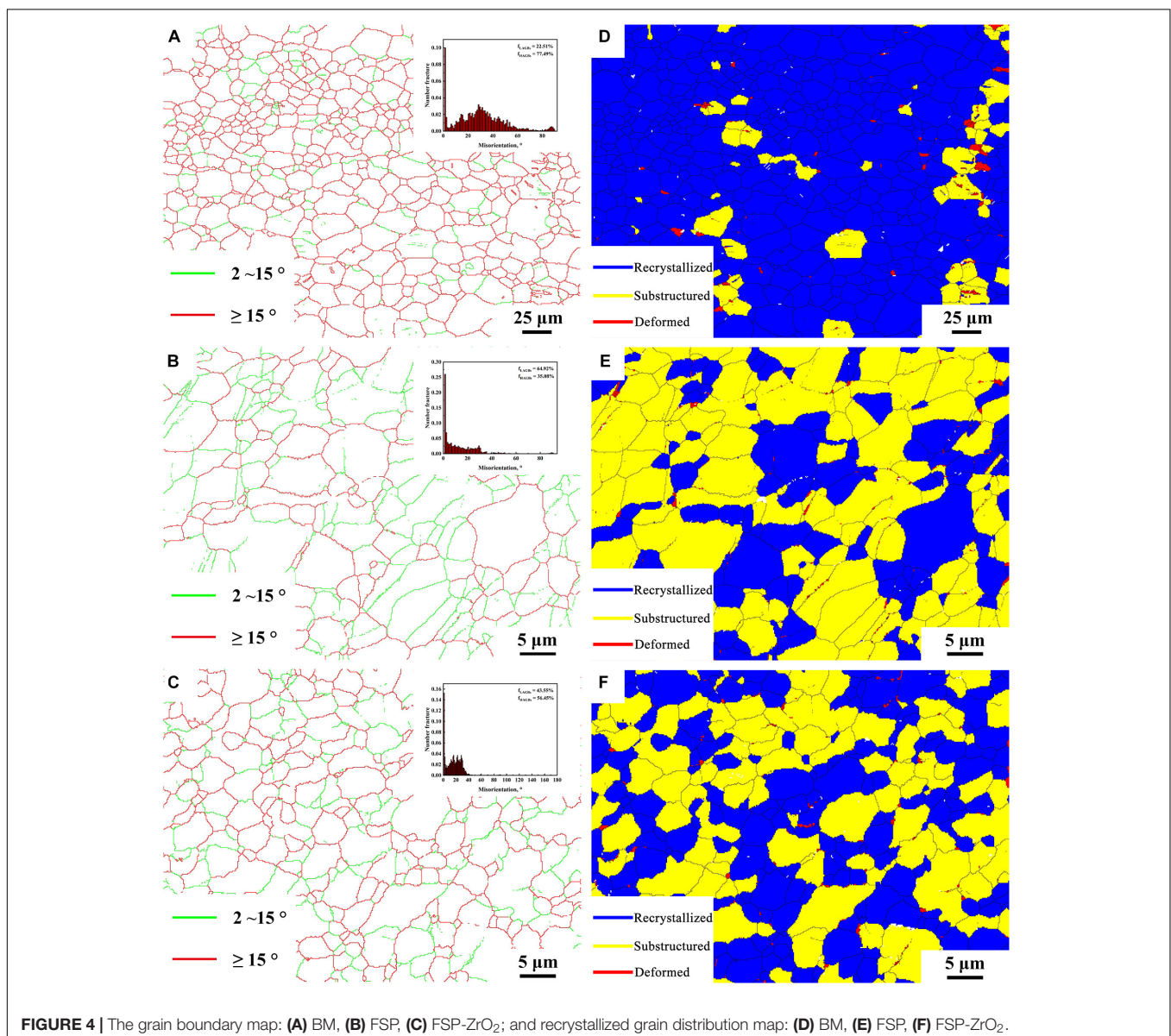

FIGURE 4 | The grain boundary map: **(A)** BM, **(B)** FSP, **(C)** FSP-ZrO$_2$; and recrystallized grain distribution map: **(D)** BM, **(E)** FSP, **(F)** FSP-ZrO$_2$.

particles are evenly distributed in the composites after FSP. **Figures 3E,F** are TEM images of FSP-ZrO$_2$ samples. It can be clearly seen that the ZrO$_2$ particles (white arrows) are well combined with the matrix, and mainly nucleate within the grains rather than preferentially distribute along the grain boundaries (red arrows). In addition, due to the high temperature and severe plastic deformation during FSP, the dislocation around the ZrO$_2$ particles is unevenly distributed, forming dislocation-rich areas (i.e., dislocation tangle) and dislocation-sparse areas (**Figure 3F**). During FSP, the stress is concentrated around the ZrO$_2$ particles due to the significant difference between the elastic modulus of the ZrO$_2$ particles and Mg matrix, thus a large number of dislocations are generated around ZrO$_2$ particles. On

the other hand, the dynamic recovery is reduced owing to the low stacking fault energy of Mg alloys, resulting in dense and sparse dislocations (Vignesh et al., 2019).
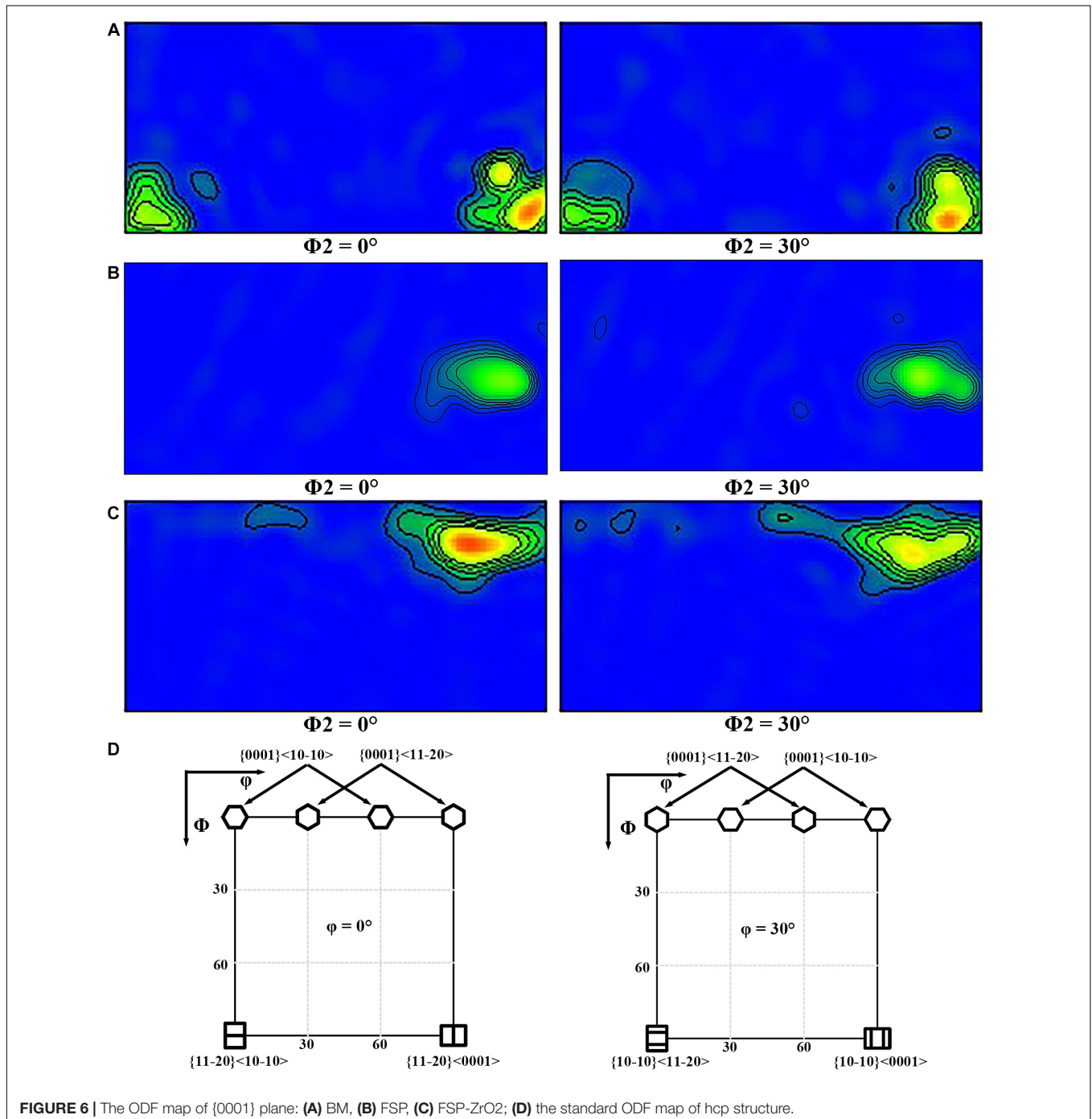
Figures 4A–F show the grain boundary distribution maps and recrystallized grain distribution maps of BM, FSP, and FSP-ZrO$_2$ samples, respectively. The insets are the misorientation angle distribution maps. The green and red lines represent low angle grain boundaries (LAGBs) of 2~15°and high angle grain boundaries (HAGBs) of >15°, respectively. Blue indicates recrystallized grains, yellow indicates sub-grains, and red indicates deformed grains. It can be seen that the proportions of HGABs in BM, FSP, and FSP-ZrO$_2$ samples are 86.3, 52.8, and 66.5%, respectively. The proportions of recrystallized grains are

FIGURE 5 | The pole figure of {0001} plane: **(A)** BM, **(B)** FSP, **(C)** FSP-ZrO$_2$.
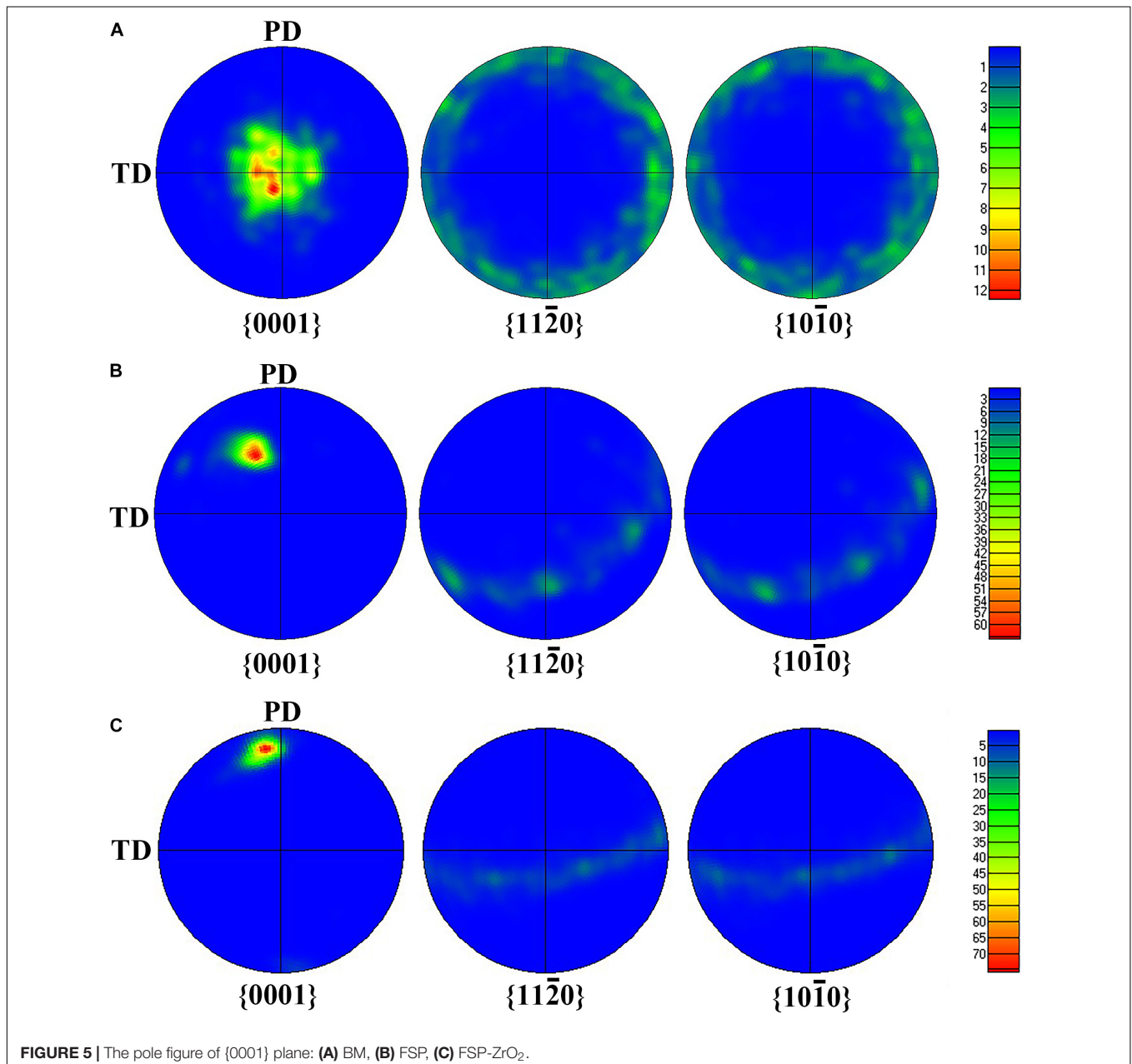
89.83, 34.37, and 48.79%, respectively. The HAGB ratios of the above three samples are all reduced because of the dislocations (**Figures 3E,F**) produced inside the grains during FSP. It is worth noting that there are a large number of 60°± 5° and 86° ± 5° twins in BM sample, 60° ± 5° twins in FSP sample are reduced, and two twins in FSP-ZrO$_2$ composites disappear, as shown in the inserts in **Figures 4A–C**. The grain size affects twin deformation, the finer the grain, the more difficult to twin. Therefore, the main reason for the reduction of twins is that FSP and the

combination of FSP with ZrO$_2$ particles makes the grain refined (**Figures 3B,C**).

Figures 5, **6** display {0001}, {11$\bar{2}$0}, and {10$\bar{1}$0} pole figures, and the {0001} orientation distribution function (ODF) map of BM, FSP, and FSP-ZrO$_2$ samples, respectively. The c-axis of {0001} plane of BM parallel to ND (**Figure 5A**), showing a typical rolled texture with the polar density of 14.63, and the texture component is {11$\bar{2}$0} < 0001 > or {10$\bar{1}$0} < 0001 > texture (**Figure 6A**). The c-axis of {0001} plane of FSP sample is deflected

FIGURE 6 | The ODF map of {0001} plane: **(A)** BM, **(B)** FSP, **(C)** FSP-ZrO2; **(D)** the standard ODF map of hcp structure.

from PD and TD approximately 45° and 80°, respectively (**Figure 5B**), and the texture component consists of $\{10\bar{1}0\}$ or $\{11\bar{2}0\}$ fiber texture with the polar density of 60.25 (**Figure 6B**). The c-axis of $\{0001\}$ plane of FSP-ZrO$_2$ sample is deflected from PD and TD approximately 15° and 85°, respectively (**Figure 5C**), and the texture component consists of $\{0001\} < 11\bar{2}0$ or $\{0001\} < 10\bar{1}0$ texture with the polar density of 77.21 (**Figure 6C**). The detailed statistical results about the texture of three samples on the $\{0001\}$ planes are shown in **Table 1**. It has been reported that the deflection of c-axis on the $\{0001\}$ plane of FSP sample is mainly due to the shear stress induced by shoulder and stir pin (Huang et al., 2019). It is worth noting that the deflection angle of c-axis of FSP-ZrO$_2$ sample is larger than that of FSP sample, which may be due to the fact that ZrO$_2$ particles increase the friction coefficient of the material during the plastic flow process, causing more grains on the $\{0001\}$ plane to deflect.

Figure 7 presents the Schmidt factor (SF) distribution of (0001) basal slip along TD and PD of BM, FSP and FSP-ZrO$_2$ specimens. The average SFs of BM, FSP, and FSP-ZrO$_2$ specimens along TD are 0.21, 0.28, and 0.17, respectively, and the average SFs along PD are 0.21, 0.45, and 0.30, respectively. BM has the same SF value along TD and PD, and both samples after FSP have different SFs along TD and PD due to the different angles between their c-axis and TD / PD. In addition, the average SF of FSP sample is higher than that of BM, and the average SF of FSP-ZrO$_2$ sample is lower than that of BM. In addition, the average SF is arranged from large to small as FSP > BM > FSP-ZrO$_2$. This indicates that FSP make material soften, while ZrO$_2$ particles make material harden. This phenomenon has been confirmed in the studies of Navazani and Dehghani (2016) and Jin et al. (2019).

Figure 8 shows the microhardness distribution of the cross section of BM, FSP, and FSP-ZrO$_2$ samples. The average microhardness of BM is 71 HV. The average microhardness of the FSP sample is reduced to 53 HV, which is mainly because the SF increases along PD (**Figures 7C,D**), causing the material to soften. The average microhardness of FSP-ZrO$_2$ samples is 99 HV, which is about 40% higher than that of BM. On the one hand, ZrO$_2$ particles further refine the grains of the Mg alloy during FSP (**Figure 3C**), and improve the strengthening effect of the refined grains. On the other hand, ZrO$_2$ particles increase the resistance of dislocation movement (Vignesh et al., 2019), so that more dislocations accumulate when the material undergoes plastic deformation (**Figures 3E,F**), thereby strengthening the matrix.

Figure 9 shows the stress-strain curves of BM, FSP, and FSP-ZrO$_2$ samples. The ultimate tensile strength (UTS) of BM, FSP,

and FSP-ZrO$_2$ samples is 283, 265, and 427 MPa, the yield strength (YS) is 137, 91, and 217 MPa, and the elongation is 15.5, 13.6, and 9.5%, respectively. Compared to BM, the YS and elongation for FSP specimens reduces, and the YS of FSP-ZrO$_2$ specimens increases by 80 MPa, while the elongation significantly reduces by about 6%. Since the ZrO$_2$ particles impede the strain around the matrix (**Figures 3E,F**), thus a plastic deformation gradient is generated on the ZrO$_2$/matrix interface, resulting in the uneven plasticity and the lower elongation for FSP-ZrO$_2$ composites. The mechanical properties of materials are usually determined by the microstructure, and detailed analysis will be discussed later. **Figure 10** shows the fracture morphology of BM, FSP, and FSP-ZrO$_2$ samples after tensile testing. It can be seen that the fracture of BM is composed of dimples with different depths and cleavage surfaces (**Figure 10A**), showing a typical quasi-cleavage fracture. The fracture of FSP sample also presents quasi-cleavage fracture characteristics, with more uniform and fewer dimples, while more cleavage surfaces (**Figure 10B**), indicating a decrease in plasticity. The fracture of FSP-ZrO$_2$ sample is composed of dimples and a small amount of cleavage surfaces (**Figure 10C**). There are a large number of ZrO$_2$ particles in the dimples (**Figure 10D**), showing the microporous aggregate fracture characteristics. This is consistent with the previous stress-strain curve results (**Figure 9**).

Electrochemical Corrosion Performance

Figure 11A shows the curves of open circuit potential (OCP) of BM, FSP and FSP-ZrO2 samples in SBF solution with time. It can be seen that the corrosion potential of the sample increases as time increases. In the initial stage of corrosion, the OCP of BM and FSP samples are similar, while the OCP of FSP-ZrO$_2$ is higher, indicating that the FSP-ZrO$_2$ sample is easier to form a passivation film and has a lower self-corrosion tendency.

Figure 11B shows the potentiodynamic polarization curves of BM, FSP, and FSP-ZrO$_2$ samples in SBF solution. The corrosion potential of BM and FSP samples are the same, while the corrosion potential of FSP-ZrO$_2$ is lower, suggesting that FSP-ZrO$_2$ samples are more sensitive to corrosion and easier to form passivation films. According to the corrosion current density, the order of samples is FSP < FSP-ZrO$_2$ < BM. Corrosion rate (P_i) that can be calculated according to Eq. (1).

$$P_i = 22.85 i_{corr} \qquad (1)$$

This means that BM presents the fastest corrosion rate and FSP sample exhibits the slowest. The results of corrosion potential (E_{corr}), corrosion current density (i_{corr}) and corrosion rate (P_i) of BM, FSP and FSP-ZrO$_2$ samples are listed in **Table 2**.

Figure 11C exhibits the Nyquist plots of BM, FSP and FSP-ZrO$_2$ samples in SBF solution. All samples are characterized by a capacitive loop in high and medium frequency range, and an inductive loop in the low frequency range. The capacitive loop is caused by the charge transfer process on the surface of the passive film, and the inductive loop is formed by the adhesion of Mg$^+$ ions and Mg(OH)$^+$ ions on the surface of the sample (Zhuang et al., 2015). FSP samples show the largest radius of capacitive and inductive loop, followed by FSP-ZrO$_2$ samples,

TABLE 1 | Detailed statistical results about the texture of three samples of $\{0001\}$ plane.

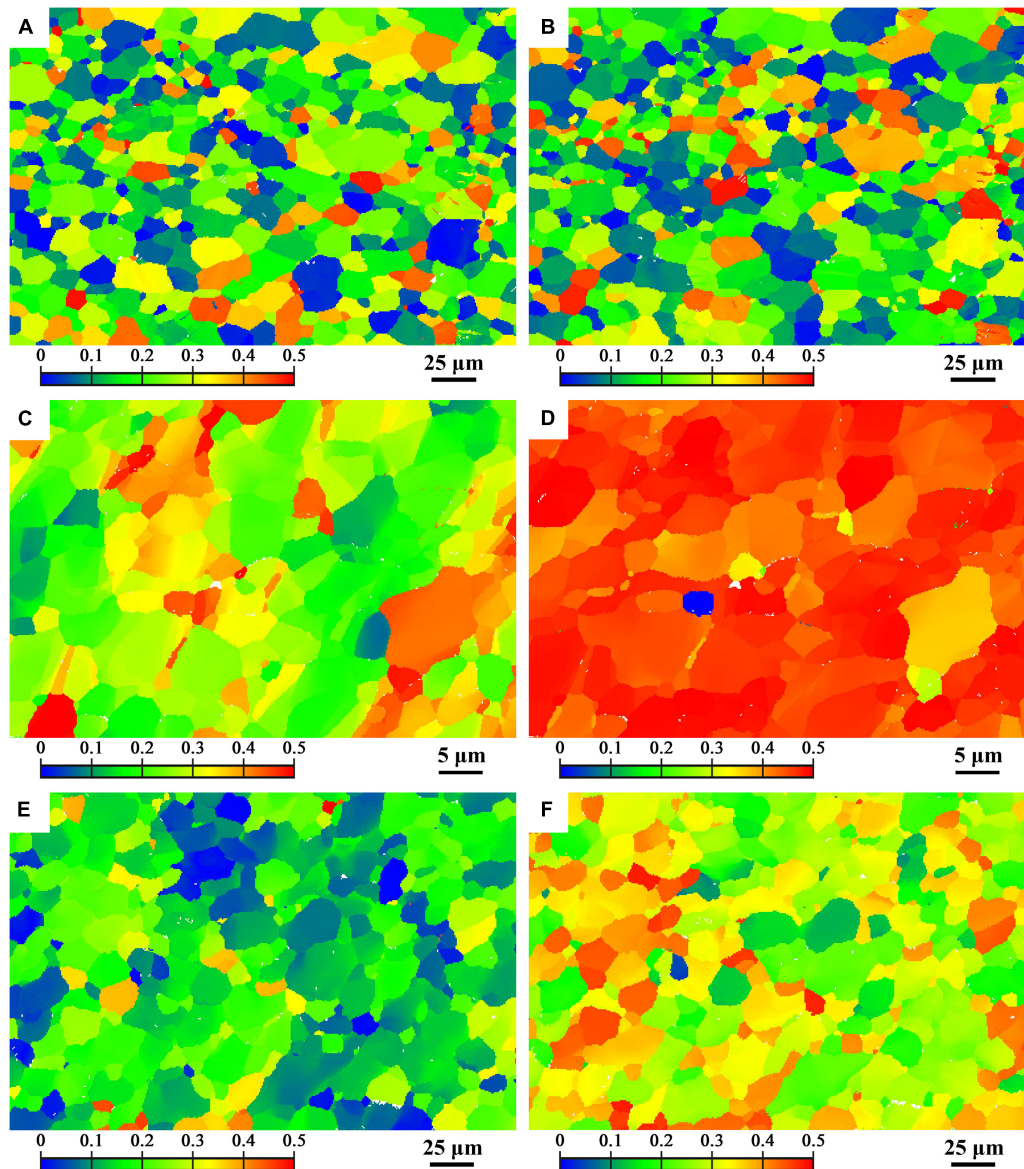| Samples	{0001}		
	The angle between c-axis and TD (°)	The angle between c-axis and PD (°)	Polar density
BM	0	90	14.63
FSP	80	45	60.25
FSP-ZrO$_2$	85	15	77.21

FIGURE 7 | Schmid factor distribution map of TD (on the left side) and PD (on the right side) of (0001) basal slip system **(A,B)** BM, **(C,D)** FSP, **(E,F)** FSP-ZrO$_2$.

and finally BM. Generally, the larger the radius of capacitive and inductive loop, the better corrosion resistance of the sample (Wang et al., 2018). Furthermore, the dislocation density at the ZrO$_2$ particles is too large (**Figures 3E,F**), and thus the local corrosion is aggravated (Liu et al., 2008). It has been reported that dislocations are easily formed between the ZrO$_2$ particles and the matrix due to a large mismatch of thermal expansion coefficient between them (ZrO$_2$ particles is $\sim$7.5 $\times$ 10^{-6} K^{-1}, Mg matrix is $\sim$27.1 $\times$ 10^{-6} K^{-1}) (Liu et al., 2008; Vedabouriswaran and Aravindan, 2018). Therefore, the FSP-ZrO$_2$ composite exhibits worse corrosion performance than FSP sample. In summary, it can be considered that the corrosion resistance of FSP samples is the best, followed by FSP-ZrO$_2$, and the corrosion resistance of BM is the worst.

SVET Voltage Maps

Figure 12 shows the SVET maps of BM, FSP and FSP-ZrO$_2$ samples soaked in SBF at 0, 1, 3, 6, and 24 h, respectively. It can be seen that a local violent reaction occurs in BM when it is just soaked in SBF, the maximum voltage is 0.122 mv. When they are soaked for 24 h, the voltage drops to 0.017 mv. The maximum voltage for FSP samples is 0.024 mv when they are just soaked in SBF, and the voltage is reduced to 0.000 mv for 24 h. The maximum voltage for FSP-ZrO$_2$ sample just immersed in SBF is −0.004 mv, and the voltage first increases and then decreases during the corrosion process. After being soaked for 24 h, the voltage drops to −0.005 mv. The above results indicate that FSP-ZrO$_2$ samples are more prone to passivation during the corrosion process, followed by FSP and BM is the worst.

FIGURE 8 | The microhardness distribution of BM, FSP and FSP-ZrO2 samples.
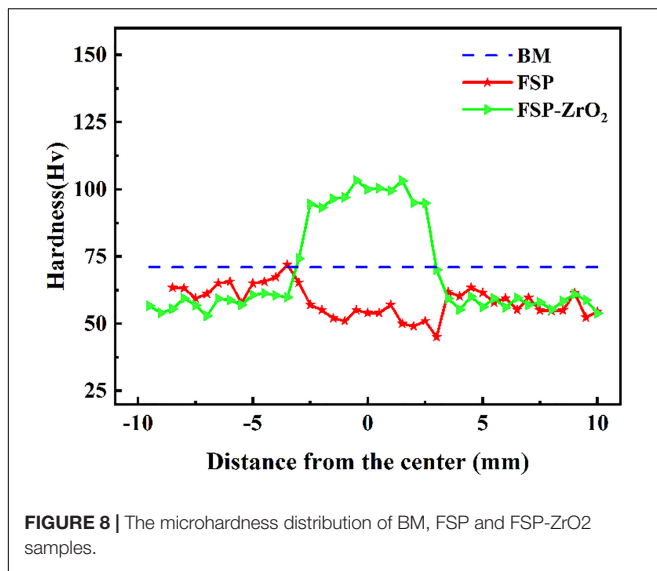
DISCUSSION

### Relationship Between Microstructure and Mechanical Property

Base metal exhibits coarse grains with inhomogeneous distribution of grain size (**Figure 3A**), while the FSP sample presents fine and uniform grains. During FSP, the effect of severe plastic deformation, high temperature and strain rate breaks the grains and causes dynamic recrystallization, resulting in the grain refinement of Mg alloy (**Figure 3B**). LAGBs entangled inside the FSP sample to form fine recrystallized grains (**Figures 4A,B**), indicating that continuous dynamic recrystallization (CDRX) occurs. Severe plastic deformation increases the dislocation density in grains, and the dislocations rotate or rearrange to form LAGBs in FSP process. These LAGBs gradually transform into HAGBs in the subsequent plastic deformation process (**Figures 4A,B**).

Compared with FSP sample, grain size of FSP-ZrO$_2$ sample is refined, and HAGBs and recrystallized grains increase (**Figures 3**, **4**). This is mainly due to the following three reasons. First, the elastic modulus of ZrO$_2$ particles is different from that of Mg matrix, which will increase dislocation density and provide more nucleation sites for CDRX during FSP (**Figures 3E,F**). Second, ZrO$_2$ particles will increase the strain and strain rate, thereby refining the grains (Mukherjee and Ghosh, 2010; Navazani and Dehghani, 2016). Third, ZrO$_2$ particles pin the dislocations, hindering the movement of dislocations and growth of grain (**Figures 3E,F**; Mazaheri et al., 2019).

In **Figures 5**, **6**, the grain orientation and texture of three samples have changed significantly. Mg alloy undergoes plastic flow under the combination of the shoulder and stirring pin during FSP, which greatly changes the grain orientation and texture (Yuan et al., 2011). From **Figure 5B**, it can be seen that the c-axis is deflected and the polar density increases for FSP sample, under the action of the compressive stress induced by the rotation of the shoulder and the shearing force of the stirring pin. For Mg alloy, basal slip has a lower critical resolved shear stress

(CRSS) compared to prismatic slip and pyramidal slip (Park et al., 2003; Woo et al., 2006). Therefore, basal slip is easier to start in FSP, resulting in the formation of obvious basal texture, and the highest polar density is four times that of BM. In addition, the deflected angle of the c-axis on the {0001} plane in FSP-ZrO$_2$ sample is larger than that of FSP sample, and the polar density is also significantly increased. This indicates that ZrO$_2$ particles contribute to the initiation of basal slip and increase the strength of basal texture.

In general, the mechanical properties of Mg alloys are mainly affected by grain size, secondary phase and grain orientation. There is hardly precipitates in AZ31 Mg alloy, so the influence of precipitates on the alloy is not considered after FSP. During FSP, the grains of the alloy are significantly refined and uniformed, while the strength is significantly lower than that of BM (**Figure 9**). The grain refinement strengthening effect is not enough to compensate for the strength loss caused by other factors. Moreover, Mg alloy undergoes severe plastic deformation during FSP, and the texture composition completely different from BM is formed in the processing zone (**Figures 5**, **6**). In addition, compared with BM, the SF value of each area for FSP sample is increased, and the basal slip is easy to proceed, so the strength of FSP sample is reduced. This reduction of strength caused by the softening of grain orientation has been confirmed in our previous studies (Wang et al., 2020). The strength of FSP-ZrO$_2$ sample is significantly higher than that of BM, as shown in **Figure 9**. Several strengthening mechanisms of composites have been proposed (Lloyd, 1994). It has been reported that increases in the YS and UTS of FSP-ZrO$_2$ composites by addition of reinforcing particles may be attributable to three factors as following (Chang et al., 2007; Navazani and Dehghani, 2016; Mazaheri et al., 2019). Firstly, the grains are obviously refined due to the dynamic recrystallization caused by FSP and the pinning effect of ZrO$_2$, triggering grain refinement strengthening (Morisada et al., 2006a; Cao et al., 2014; Sun et al., 2017). Secondly, ZrO$_2$ particles uniformly distributed in the matrix are pinned to the grain boundaries, hindering the movement
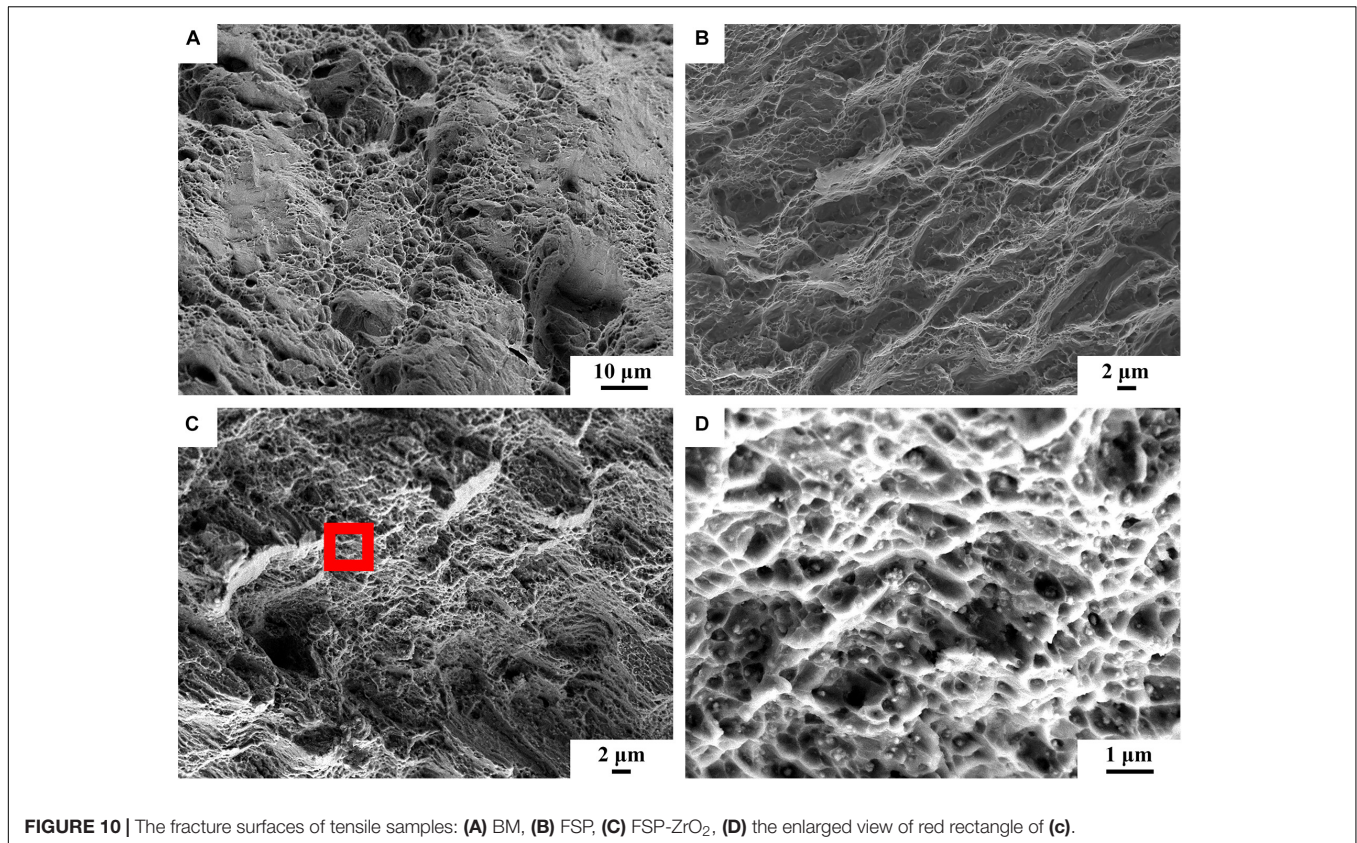

FIGURE 9 | The stress-strain curves of BM, FSP and FSP-ZrO$_2$ samples.
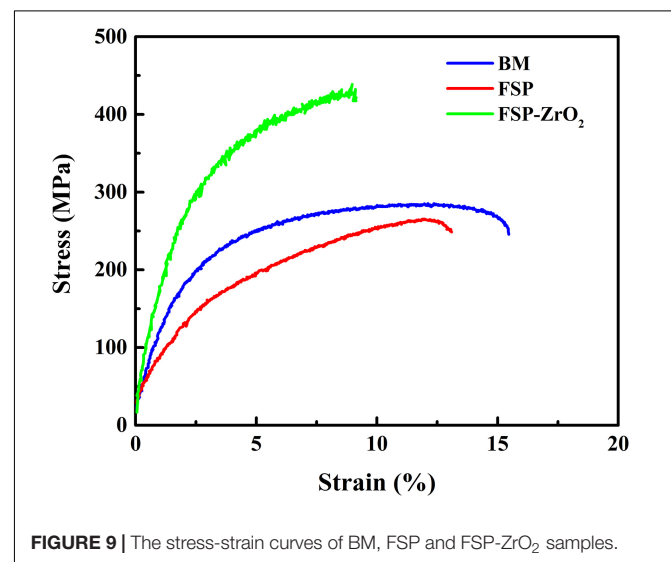
FIGURE 10 | The fracture surfaces of tensile samples: **(A)** BM, **(B)** FSP, **(C)** FSP-ZrO$_2$, **(D)** the enlarged view of red rectangle of **(c)**.

of dislocations and causing Orowan strengthening. Thirdly, the load-transfer strengthening caused by the difference in elastic modulus between Mg matrix and ZrO$_2$ particles.

Furthermore, the contribution of each strengthening mechanism to the YS of FSP-ZrO$_2$ composites can be calculated using the mathematical equations as following (Hall, 1951; Zhang and Chen, 2006; Shahin et al., 2019):

$$\sigma_y = \sigma_0 + k_y d^{-1/2} \tag{2}$$

where σ_s is the yield strength, σ_0 is the friction stress, k_y is the stress concentration factor (5 MPa mm$^{1/2}$), and d is the average grain size.

$$\sigma_{orowan} = \sqrt{3}\frac{Gb}{L} \tag{3}$$

where G is the shear modulus (1.64 × 10^4 MPa), b is Burgers vector (3.21 × 10^{-10} m), L is the average distance between ZrO$_2$ particles (350 nm).

$$\sigma_{LT} = \frac{\sigma_{my}f_v}{2} \tag{4}$$

where σ_{my} is the YS of BM (137 MPa), f_v is the volume fraction of ZrO$_2$ particles (about 17.6%).
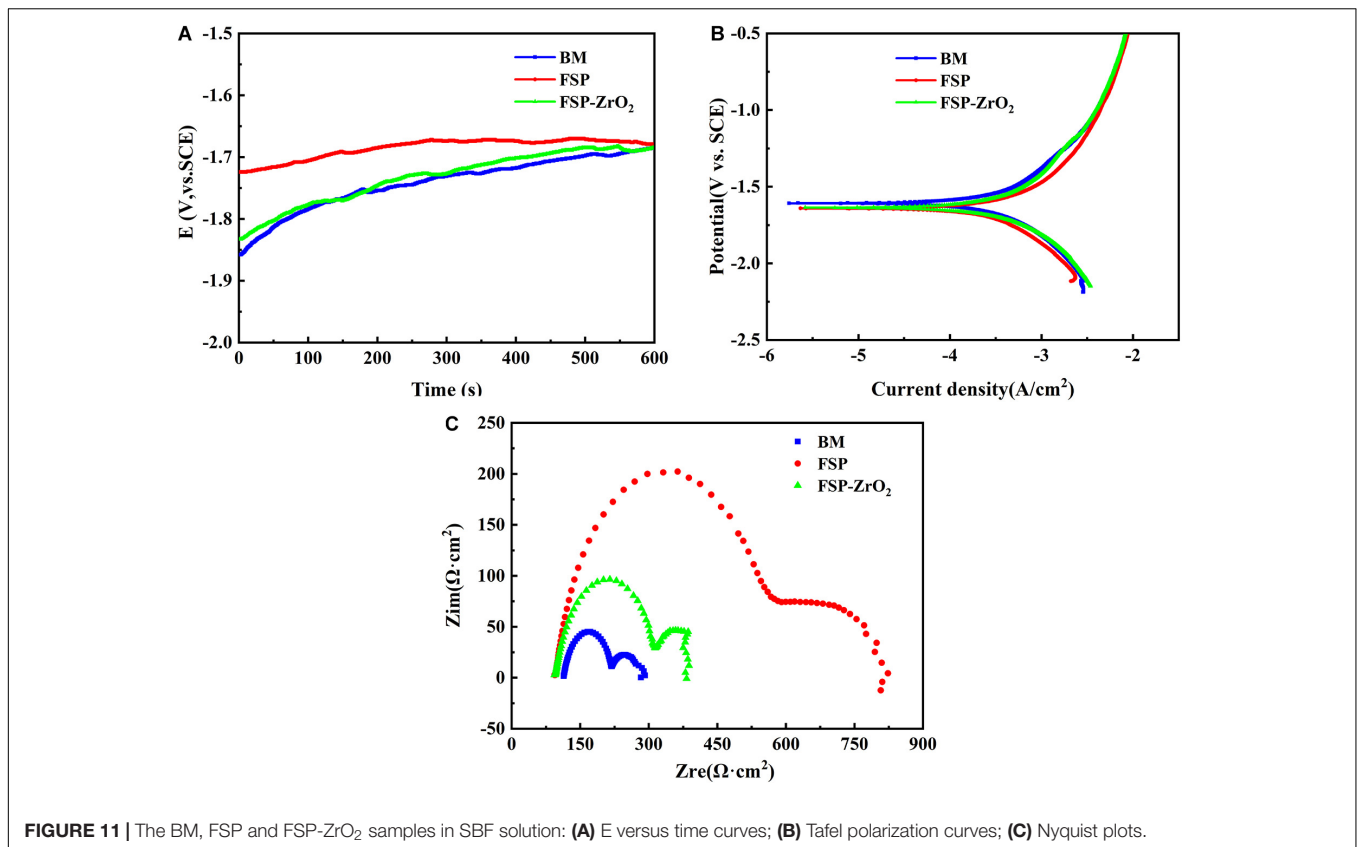
Based on Eqs. (2) – (4), the calculated strength increments between the as-received AZ31 and FSP-ZrO$_2$ samples were about 39.8, 26.8, and 12.1 MPa, respectively. This indicates that grain refinement strengthening contributes to improve the strength of the material, followed by Orowan strengthening, and finally load transfer strengthening. This is because the reduction of the grain size for metal matrix directly effects the increase of the strength characteristics of specimens after uniaxial tensile (Vedabouriswaran and Aravindan, 2018). Saikrishna et al. (2017) also proposed the similar conclusion. In addition, the size of the reinforcement particle (Orowan strengthening) contributes in the improvement of strength. Therefore, FSP-ZrO$_2$ sample in this work presents the highest UTS and YS. Adding the contributions of various strength mechanisms, the strength increment of the material is 78.7 MPa, whereas the measured strength increment is approximately 80 MPa (**Figure 9**). This indicates a good agreement between the calculated and measured amounts of strength. In conclusion, the grain refinement and Orowan strengthening mechanism can be considered as the major reason of the enhanced strength for FSP-ZrO$_2$ sample in this work.

Corrosion Mechanism of the FSP-ZrO$_2$

As shown in **Figure 11B**, BM, FSP samples and FSP-ZrO$_2$ composites exhibit similar cathodic reaction and anodic dissolution characteristics. It is known that Mg and its alloys suffer electrochemical corrosion in aqueous solutions, involving cathodic reduction of water (5) and anodic dissolution of Mg (6) (Esmaily et al., 2016).

$$2H_2O + 2e^- \rightarrow H_2 \uparrow 2OH^- \tag{5}$$

$$Mg \rightarrow Mg^{2+} + 2e^- \tag{6}$$

FIGURE 11 | The BM, FSP and FSP-ZrO$_2$ samples in SBF solution: **(A)** E versus time curves; **(B)** Tafel polarization curves; **(C)** Nyquist plots.

According to Eqs. (5) and (6), the overall corrosion reaction (7) during electrochemical corrosion processing as following:

$$Mg + 2H_2O = Mg(OH)_2 + H_2 \uparrow \qquad (7)$$
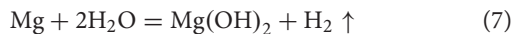
Mg dissociates in aqueous environments to form Mg hydroxide ($Mg(OH)_2$) and hydrogen (H_2) gas. The $Mg(OH)_2$ corrosion film product formed on the alloy surface is a very poor electronic conductor and the rate of corrosion is hence strongly reduced (Esmaily et al., 2016).

The electrochemical corrosion test and SVET measurement of BM, FSP, and FSP-ZrO$_2$ samples were carried out (**Figures 11**, **12**) in this work. In both tests, the corrosion rate of FSP-ZrO$_2$ sample is lower than that of BM (**Table 2**), which indicates that it has better corrosion resistance. In the electrochemical corrosion test, the corrosion resistance of FSP sample is better than that of FSP-ZrO$_2$ sample, while the opposite result appears in the SVET measurement. For Mg alloys, grain size and grain orientation are the main factors affecting their corrosion resistance (Huang et al., 2019). For Mg matrix composites, in addition to the above two factors, reinforced particles also affect the corrosion resistance significantly (Vignesh et al., 2019).

Generally, grain refinement is considered to effectively improve the corrosion resistance of Mg alloys (Saikrishna et al., 2017; Wang et al., 2018; Huang et al., 2019). The corrosion resistance depends on the grain size, via the grain boundary defects. The high grain boundary energy and chemical activity promote rapid transfer rate of electrons and materials, resulting

in a strong chemical reaction, so the grain boundary can provide more nucleation sites for the passive film. Fine-grained structure can provide more grain boundaries, and the smaller grain size can promote the formation of the protective $Mg(OH)_2$ layer. Moreover, Choi and Kim (2015) reported that the grain boundary is conducive to stress release and can reduce the number of cracks in the protective film or corrosion layer. Therefore, grain refinement can improve the biological corrosion resistance of Mg alloy. In constant, it has been reported that the grain refinement and the increase of grain boundaries are harmful to corrosion properties. Because of the high defect density at the grain boundary, the material has a greater tendency to corrosion. According to **Figures 11**, **12**, the grain size of FSP and FSP-ZrO$_2$ samples in this study is smaller than that of BM, which means that they have better corrosion resistance, so it can be considered that grain refinement contributes to improve the corrosion resistance of FSP-ZrO$_2$ composites.

On the other hand, grain orientation is also a critical factor for influencing the corrosion behavior of FSP-ZrO$_2$ composites.

TABLE 2 | The results of E_{corr}, i_{corr} and P_i of samples in SBF solution.

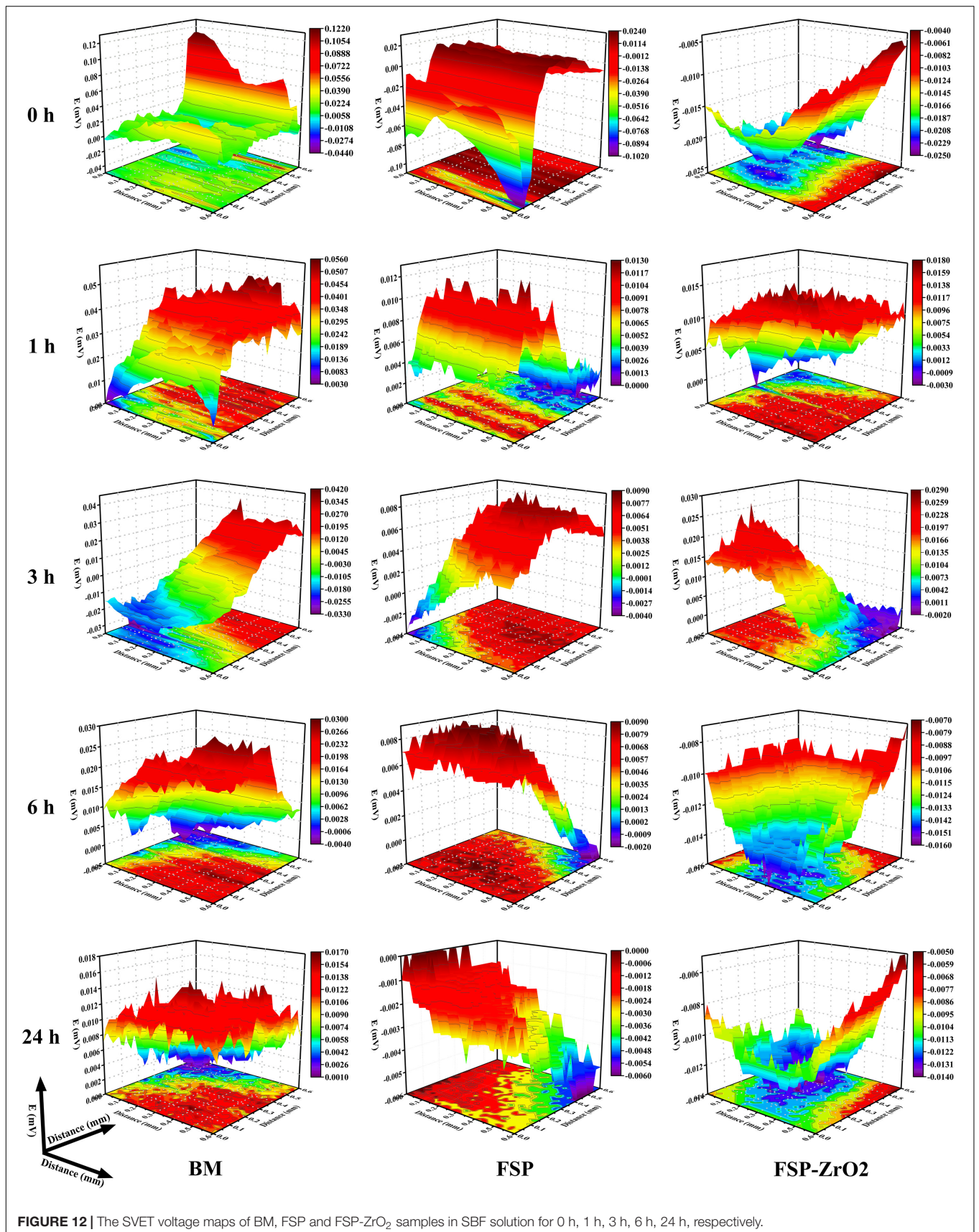| Sample	E_{corr} (V)	i_{corr} (mA/cm^2)	P_i (mm/y)
BM	−1.61 ± 0.02	0.271 ± 0.003	6.19 ± 0.02
FSP	−1.61 ± 0.01	0.090 ± 0.002	2.06 ± 0.04
FSP-ZrO$_2$	−1.64 ± 0.01	0.217 ± 0.001	4.96 ± 0.02

FIGURE 12 | The SVET voltage maps of BM, FSP and FSP-ZrO$_2$ samples in SBF solution for 0 h, 1 h, 3 h, 6 h, 24 h, respectively.

Previous studies have shown that the (0001) plane of Mg alloy is more resistant to corrosion than (10–10) and (11–20) plane (Liu et al., 2008; Campo et al., 2014; Huang et al., 2019). The (0001) plane of Mg alloy exhibits the highest atomic density (1.13×10^{19}, atom/m^2) and the lowest surface energy, which leads to a low atomic dissolution rate during the corrosion. Besides, Micro-zone primary cells are formed between different grain orientations, which in turn affects the OCP (Song et al., 2010). In this study, the micro-galvanic effect in FSP and FSP-ZrO$_2$ samples leads to preferential dissolution of grains with (10–10) and (11–20) orientations, resulting in the increase of OCP (**Figure 11A**), thus improving the corrosion resistance of the materials.

In addition, the effect of ZrO$_2$ particles on the corrosion performance of FSP-ZrO$_2$ sample cannot be ignored. The secondary particles improve the corrosion resistance of Mg alloy mainly in the following two ways. One is to promote grain refinement, and the other is to play a role in obstacle. According to the previous experimental results (**Figures 3, 4**), adding ZrO$_2$ particles into AZ31 Mg with FSP can promote grain refinement, and then improve the corrosion performance. Similar results have been reported (Esmaily et al., 2016; Wang et al., 2018; Huang et al., 2019). Moreover, Vignesh et al. (2019) believed that the dispersion distribution of ZrO$_2$ particles in composites increases the cumulative corrosion potential of the material, which increases the corrosion resistance of the composite. Mensah-Darkwa et al. (2013) studied the corrosion properties of Mg-hydroxyapatite (HA) composites and found that HA provides greater resistance to electrons and ions on the surface of Mg, so it essentially has greater corrosion resistance. In this study, during the corrosion process of FSP-ZrO$_2$ sample, there are many dislocations (**Figures 3E,F**) around ZrO$_2$ particles. Corrosion is more likely to occur at the position where the dislocation intersects the surface of the matrix (Liu et al., 2008). Therefore, ZrO$_2$ particles can be used as obstacles to effectively prevent the penetration of corrosion and ultimately improve the corrosion resistance of the alloy. It is reported that reinforced particles can also reduce the corrosion resistance of the composites (Liu et al., 2008). For example, Saikrishna et al. (2017) prepared MWCNT/Mg composites by FSP, but its corrosion resistance was reduced because the added carbon nanotubes provide a nucleation site for galvanic corrosion. Meanwhile, this effect suppresses the effect of grain size and grain orientation on corrosion properties.

In summary, grain size, ZrO$_2$ particles and grain orientation all influence the corrosion properties. Among them, the grain size is the main factor affecting the corrosion performance. According to the microstructure results, the size of FSP-ZrO$_2$ (3.2 μm) is smaller than that of FSP (4 μm) and should have better corrosion resistance, which had been confirmed by SVET measurement (**Figure 11**). However, its electrochemical corrosion performance is lower than that of FSP sample, which may be due to the stress concentration caused by the pits left by the shedding of ZrO$_2$ particles, which accelerates the corrosion rate. When the grain size is similar, ZrO$_2$ particles are easy to fall off and affect the corrosion performance. In addition, grain orientation has little effect on the corrosion performance because it affects the corrosion performance by affecting the surface energy.

CONCLUSION

(1) AZ31/ZrO$_2$ composites with fine, densified and homogenized microstructure can be prepared by FSP. The grain size is refined from 10 μm of BM to 3.2 μm. After FSP, a strong basal texture is produced, and the c-axis of the grain is deflected under the action of compressive stress of shoulder and shear stress of pin.

(2) With the addition of ZrO$_2$ particles, the microhardness of FSP-ZrO$_2$ composites increases from 71 HV (BM) to 99 HV, UTS from 273 MPa (BM) to 427 MPa, YS from 137 MPa (BM) to 217 MPa. The strengthening mechanisms of the composites are mainly fine grain strengthening and Orowan strengthening. Compared with BM, the addition of ZrO$_2$ particles increase the brittleness but decrease the elongation. BM and FSP samples show quasi-cleavage fracture characteristics, while FSP-ZrO$_2$ composites present microporous polymerization fracture characteristics.

(3) The electrochemical corrosion behavior of three samples in SBF solution shows that the i_{corr} of FSP-ZrO$_2$ composites decreases and the radius of capacitive loop increases, indicating that the corrosion rate decreases but the corrosion resistance increases for the composites. The main factors affecting the corrosion performance are grain size and ZrO$_2$ particles.

DATA AVAILABILITY STATEMENT

The raw data supporting the conclusions of this article will be made available by the authors, without undue reservation.

AUTHOR CONTRIBUTIONS

KQ and TZ performed the experiments and wrote the manuscript. SY and SZ designed the research. ZW and PP analyzed the data. JC analyzed the data and reviewed the manuscript. LW, CL, and WW contributed to the design and data analysis. All authors read and approved the final manuscript.

FUNDING

REFERENCES

Ammouri, A. H., Kridli, G., Ayoub, G., and Hamade, R. F. (2015). Relating grain size to the Zener–Hollomon parameter for twin-roll-cast AZ31B alloy refined by friction stir processing. *J. Mater. Process. Technol.* 222, 301–306. doi: 10.1016/j.jmatprotec.2015.02.037

Arab, S. M., Zebarjad, S. M., and Jahromi, S. A. J. (2017). Fabrication of AZ31/MWCNTs surface metal matrix composites by friction stir processing: investigation of microstructure and mechanical properties. *J. Mater. Eng. Perform.* 26, 5366–5374. doi: 10.1007/s11665-017-2763-y

Azizieh, M., Larki, A. N., Tahmasebi, M., Bavi, M., Alizaden, E., and Kim, H. S. (2018). Wear behavior of AZ31/Al$_2$O$_3$ magnesium matrix surface nanocomposite fabricated via friction stir processing. *J. Mater. Eng. Perform.* 27, 2010–2017. doi: 10.1007/s11665-018-3277-y

Balakrishnan, M., Dinaharan, I., Palanivel, R., and Sivaprakasam, R. (2015). Synthesize of AZ31/TiC magnesium matrix composites using friction stir processing. *J. Magnes. Alloy.* 3, 76–78. doi: 10.1016/j.jma.2014.12.007

Campo, R., Savoini, B., Muñoz, A., Monge, M. A., and Garcés, G. (2014). Mechanical properties and corrosion behavior of Mg-HAP composites. *J. Mech. Behav. Biomed. Mater.* 39, 238–246. doi: 10.1016/j.jmbbm.2014.07.014

Cao, L., Liu, W. C., Li, Z. Q., Wu, G. H., Xiao, L., Wang, S. H., et al. (2014). Effect of heat treatment on microstructures and mechanical properties of sand-cast Mg-10Gd-3Y-0.5Zr magnesium alloy. *Trans. Nonferrous Met. Soc. China* 24, 611–618. doi: 10.1016/S1003-6326(14)63102-2

Castellani, C., Lindtner, R. A., Hausbrandt, P., Tschegg, E., Tschegg, S. E. S., Zanoni, G., et al. (2011). Bone–implant interface strength and osseointegration: biodegradable magnesium alloy versus standard titanium control. *Acta Biomater.* 7, 432–440. doi: 10.1016/j.actbio.2010.08.020

Chang, C. I., Wang, Y. N., Pei, H. R., Lee, C. J., Du, X. H., and Huang, J. C. (2007). Microstructure and mechanical properties of nano-ZrO$_2$ and nano-SiO$_2$ particulate reinforced AZ31-Mg based composites fabricated by friction stir processing. *Key Eng. Mater.* 351, 114–119. doi: 10.4028/www.scientific.net/KEM.351.114

Choi, H. Y., and Kim, W. J. (2015). Effect of thermal treatment on the bio-corrosion and mechanical properties of ultrafine-grained ZK60 magnesium alloy. *J. Mech. Behav. Biomed. Mater.* 51, 291–301. doi: 10.1016/j.jmbbm.2015.07.019

Daniel, B. S. S., Murthy, V. S. R., and Murty, G. S. (1997). Metal-ceramic composites via in-situ methods. *J. Mater. Process. Technol.* 68, 132–155. doi: 10.1016/S0924-0136(96)00020-9

Davis, E. A., and Ward, I. M. (1993). *An Introduction to Metal Matrix Composites*. New York, NY: Cambridge University Press.

Esmaily, M., Mortazavi, N., Svensson, J. E., Halvarsson, M., Jarfors, A. E. W., Wessén, M., et al. (2016). On the microstructure and corrosion behavior of AZ91/SiC composites produced by rheocasting. *Mater. Chem. Phys.* 180, 29–37. doi: 10.1016/j.matchemphys.2016.05.016

Gobara, M., Shamekh, M., and Akid, R. (2015). Improving the corrosion resistance of AZ91D magnesium alloy through reinforcement with titanium carbides and borides. *J. Magnes. Alloy.* 39, 112–120. doi: 10.1016/j.jma.2015.03.002

Hall, E. O. (1951). The deformation and ageing of mild steel: III discussion of results. *Proc. Phys. Soc. B* 64:747. doi: 10.1088/0370-1301/64/6/305

Hashim, J., Looney, L., and Hashmi, M. S. J. (1999). Metal matrix composites: production by the stir casting method. *J. Mater. Process. Technol.* 92–93, 1–7. doi: 10.1016/S0924-0136(99)00118-1

Henderson, S. E., Verdelis, K., Maiti, S., Pal, S., Chung, W. L., Chou, D. T., et al. (2014). Magnesium alloys as a biomaterial for degradable craniofacial screws. *Acta Biomater.* 10, 2323–2332. doi: 10.1016/j.actbio.2013.12.040

Huang, L. Y., Wang, K. S., Wang, W., Peng, P., Qiao, K., and Liu, Q. (2019). Microstructural evolution and corrosion behavior of friction stir processed fine-grained AZ80 Mg alloy. *Mater. Corros.* 71, 93–108. doi: 10.1002/maco.201911108

Jin, Y. Y., Wang, K. S., Wang, W., Peng, P., Zhou, S., Huang, L. Y., et al. (2019). Microstructure and mechanical properties of AE42 rare earth-containing magnesium alloy prepared by friction stir processing. *Mater. Charact.* 150, 52–61. doi: 10.1016/j.matchar.2019.02.008

Kokubo, T., and Takadama, H. (2006). How useful is SBF in predicting in vivo bone bioactivity? *Biomaterials* 27, 2907–2915. doi: 10.1016/j.biomaterials.2006.01.017

Lan, J., Yang, Y., and Li, X. (2004). Microstructure and microhardness of SiC nanoparticles reinforced magnesium composites fabricated by ultrasonic method. *Mater. Sci. Eng. A* 386, 284–290. doi: 10.1016/j.msea.2004.07.024

Lavernia, E. J., and Grant, N. J. (1988). Spray deposition of metals: a review. *Mater. Sci. Eng.* 98, 381–394. doi: 10.1016/0025-5416(88)90191-7

Liu, M., Qiu, D., Zhao, M. C., Song, Gl, and Atrens, A. (2008). The effect of crystallographic orientation on the active corrosion of pure magnesium. *Scr. Mater.* 58, 421–424. doi: 10.1016/j.scriptamat.2007.10.027

Lloyd, D. J. (1994). Particle reinforced aluminium and magnesium matrix composites. *Int. Mater. Rev.* 39, 1–23. doi: 10.1179/095066094790150982

Mazaheri, Y., Jalilvand, M. M., Heidarpour, A., and Jahani, R. A. (2019). Tribological behavior of AZ31/ZrO$_2$ surface nanocomposites developed by friction stir processing. *Tribol. Int.* 143:106062. doi: 10.1016/j.triboint.2019.106062

Mensah-Darkwa, K., Gupta, R. K., and Kumar, D. (2013). Mechanical and corrosion properties of magnesiume-hydroxyapatite (Mg-HA) composite thin films. *J. Mater. Sci. Technol.* 29, 788–794. doi: 10.1016/j.jmst.2013.04.019

Mishra, R. S., and Ma, Z. Y. (2005). Friction stir welding and processing. *Mater. Sci. Eng. R* 50, 1–78. doi: 10.1016/j.mser.2005.07.001

Morisada, Y., Fujii, H., Nagaoka, T., and Fukusumi, M. (2006a). Effect of friction stir processing with SiC particles on microstructure and hardness of AZ31. *Mater. Sci. Eng. A* 433, 50–54. doi: 10.1016/j.msea.2006.06.089

Morisada, Y., Fujii, H., Nagaoka, T., and Fukusumi, M. (2006b). MWCNTs/AZ31 surface composites fabricated by friction stir processing. *Mater. Sci. Eng. A* 419, 344–348. doi: 10.1016/j.msea.2006.01.016

Mukherjee, S., and Ghosh, A. K. (2010). Flow visualization and estimation of strain and strain-rate during friction stir process. *Mater. Sci. Eng. A* 527, 5130–5135. doi: 10.1016/j.msea.2010.04.091

Navazani, M., and Dehghani, K. (2015). Investigation of microstructure and hardness of Mg/TiC surface composite fabricated by Friction Stir Processing (FSP). *Proc. Mater. Sci.* 11, 509–514. doi: 10.1016/j.mspro.2015.11.082

Navazani, M., and Dehghani, K. (2016). Fabrication of Mg-ZrO$_2$ surface layer composites by friction stir processing. *J. Mater. Process. Technol.* 229, 439–449. doi: 10.1016/j.jmatprotec.2015.09.047

Ni, D. R., Wang, J. J., and Ma, Z. Y. (2016). Shape memory effect, thermal expansion and damping property of friction stir processed NiTip/Al composite. *J. Mater. Sci. Technol.* 32, 162–166. doi: 10.1016/j.jmst.2015.12.013

Park, S. H. C., Sato, Y. S., and Kokawa, H. (2003). Basal plane texture and flow pattern in friction stir weld of a magnesium alloy. *Metall. Mater. Trans. A* 34, 987–994. doi: 10.1007/s11661-003-0228-4

Saikrishna, N., Pradeep, K. R. G., Munirathinam, B., Ravikumar, D., Jagannatham, M., and Sunil, B. R. (2017). An investigation on the hardness and corrosion behavior of MWCNT/Mg composites and grain refined Mg. *J. Magnes. Alloy.* 6, 83–89. doi: 10.1016/j.jma.2017.12.003

Shahin, M., Munir, K., Wen, C., and Li, Y. (2019). Magnesium matrix nanocomposites for orthopedic applications: a review from mechanical, corrosion, and biological perspectives. *Acta Biomater.* 96, 1–19. doi: 10.1016/j.actbio.2019.06.007

Song, G. L., Mishra, R., and Xu, Z. Q. (2010). Crystallographic orientation and electrochemical activity of AZ31 Mg alloy. *Electrochem. Commun.* 12, 1009–1012. doi: 10.1016/j.elecom.2010.05.011

Staiger, M. P., Pietak, A. M., Huadmai, J., and Dias, G. (2006). Magnesium and its alloys as orthopedic biomaterials: a review. *Biomaterials* 27, 1728–1734. doi: 10.1016/j.biomaterials.2005.10.003

Sun, J., Zhang, D. F., Tang, T., Yu, D. L., Xu, J. Y., and Pan, F. H. (2017). Effect of aging treatment before extrusion on microstructure and mechanical properties of AZ80 magnesium alloy. *Rare Metal Mater. Eng.* 46, 1768–1774. doi: 10.1016/S1875-5372(17)30164-9

Ugandhar, S., Gupta, M., and Sinha, S. K. (2006). Enhancing strength and ductility of Mg/SiC composites using recrystallization heat treatment. *Compos. Struct.* 72, 266–272. doi: 10.1016/j.compstruct.2004.11.010

Vedabouriswaran, G., and Aravindan, S. (2018). Development and characterization studies on magnesium alloy (RZ 5) surface metal matrix composites through friction stir processing. *J. Magnes. Alloy.* 6, 145–163. doi: 10.1016/j.jma.2018.03.001

Vignesh, R. V., Padmanaban, R., Govindaraju, M., and Priyadharshini, S. G. (2019). Investigations on the corrosion behaviour and biocompatibility of magnesium

alloy surface composites AZ91D-ZrO$_2$ fabricated by friction stir processing. *Trans. Inst. Metal Finish.* 97, 261–270. doi: 10.1080/00202967.2019.1648005

Wang, H. Y., Jiang, Q. C., Wang, Y., Ma, B. X., and Zhao, F. (2004). Fabrication of TiB$_2$ particulate reinforced magnesium matrix composites by powder metallurgy. *Mater. Lett.* 58, 3509–3513. doi: 10.1016/j.matlet.2004.04.038

Wang, W., Han, P., Peng, P., Zhang, T., Liu, Q., Yuan, S. N., et al. (2020). Friction stir processing of magnesium alloys: a review. *Acta Metall. Sin.* 33, 43–57. doi: 10.1007/s40195-019-00971-7

Wang, W., Xu, R. Q., Hao, Y. X., Wang, Q., Yu, L. L., Che, Q. Y., et al. (2018). Corrosion fatigue behavior of friction stir processed interstitial free steel. *J. Mater. Sci. Technol.* 34, 148–156. doi: 10.1016/j.jmst.2017.11.013

Woo, W., Choo, H., Brown, D. W., Liaw, P. K., and Feng, Z. (2006). Texture variation and its influence on the tensile behavior of a friction-stir processed magnesium alloy. *Scr. Mater.* 54, 1859–1864. doi: 10.1016/j.scriptamat.2006.02.019

Xu, N., and Bao, Y. (2016). Enhanced mechanical properties of tungsten inert gas welded AZ31 magnesium alloy joint using two-pass friction stir processing with rapid cooling. *Mater. Sci. Eng. A* 655, 292–299. doi: 10.1016/j.msea.2016.01.009

Yuan, W., Mishra, R. S., Carlson, B., Mishra, R. K., Verma, R., and Kubic, R. (2011). Effect of texture on the mechanical behavior of ultrafine grained magnesium alloy. *Scr. Mater.* 64, 580–583. doi: 10.1016/j.scriptamat.2010.11.052

Zhang, Z., and Chen, D. L. (2006). Consideration of Orowan strengthening effect in particulate-reinforced metal matrix nanocomposites: a model for predicting their yield strength. *Scr. Mater.* 54, 1321–1326. doi: 10.1016/j.msea.2006.10.184

Zhuang, J. J., Guo, Y. Q., Xiang, N., Xiong, Y., Hu, Q., and Song, R. G. (2015). A study on microstructure and corrosion resistance of ZrO$_2$-containing PEO coatings formed on AZ31 Mg alloy in phosphate-based electrolyte. *Appl. Surf. Sci.* 357(Pt B), 1463–1471. doi: 10.1016/j.apsusc.2015.10.025